

Time–Temperature–Transformation (TTT) Diagrams for Crystallization of Metal Oxide Thin Films

By Jennifer L. M. Rupp,* Barbara Scherrer, Nina Schäuble, and Ludwig J. Gauckler

Time–temperature–transformation (TTT) diagrams are proposed for the crystallization of amorphous metal oxide thin films and their specific characteristics are discussed in comparison to glass-based materials, such as glass-ceramics and metallic glasses. The films crystallize from amorphous to full crystallinity in the solid state. As an example the crystallization kinetics for a single-phase metal oxide, ceria, and its gadolinia solid solutions are reported made by the precipitation thin-film method spray pyrolysis. The crystallization of an amorphous metal oxide thin film generally follows the Lijsschitz–Sletow–Wagner (LSW) Ostwald ripening theory: Below the percolation threshold of 20 vol% single grains crystallize in the amorphous phase and low crystallization rates are measured. In this state no impact of solute on crystallization is measurable. Once the grains form primary clusters above the threshold the solute slows down crystallization (and grain growth) thus shifting the TTT curves of the doped ceria films to longer times and higher temperatures in comparison to undoped ceria. Current views on crystallization of metal oxide thin films, the impact of solute dragging, and primary TTT diagrams are discussed. Finally, examples on how to use these TTT diagrams for better thermokinetic engineering of metal oxide thin films for MEMS are given, for example, for micro-Solid Oxide Fuel Cells and resistive sensors. In these examples the electrical properties depend on the degree of crystallinity and, thereby, on the TTT conditions.

1. Introduction

In materials science, time–temperature–transformation (TTT) diagrams express the conversion rates of equal phase transformations during cooling.^[1] The most prominent materials for which TTT diagrams are used are steels, alloys,^[2] metallic glasses,^[3,4] glasses, and glass-ceramics.^[5–9] They all have in common that their history of phase formation is dependent on their cooling rate. A primary TTT diagram was produced for steel to predict the formation and existence of martensite and bainite during melt cooling depending on the cooling rate.^[10] The processing of glass-based materials depends specifically on TTT diagrams to predict characteristics such as vitrification,

nucleation states, and the conversion to distinctive degrees of crystallinity with respect to the undercooling history of the glass melt. In general, the curves in TTT diagrams exhibit a “C-type” form with respect to the temperature–time ordinates, as shown schematically in **Figure 1** for metal- and glass-based systems. Thereby, the nose of the TTT-curve points towards the ordinates. This “C-type” curve shape is given by the increase in driving force for crystallization with decreasing temperature of the melt and the concurrent decrease in atomic mobility of the material.^[3,7] Thus, the nose defines through its temperature T_n the minimum cooling rate for which phase transformation occurs.^[1,7] Uhlmann correlated the melting temperature T_m to the nose temperature T_n , which is also indirectly correlated to the viscosity of the material through the Vogel-Fulcher relation.^[11,12] For alloys and solid-solution strengthened glasses the nose of the TTT curve is shifted to the right, thus providing more time to undergo phase transition. This TTT kinetic approach allows the minimal cooling rate and the general temperature–time dependence for the phase transfor-

mation, in general from the amorphous (or glassy) state to the crystalline state, to be estimated.

Recently, amorphous metal oxide thin films have been reported to exhibit similar crystallization kinetic rules and characteristics as glass-based systems,^[13] for instance, Kissinger crystallization activation energies between 1–3 eV,^[14] Johnson-Mehl-Avrami characteristics,^[15,16] and crystallization enthalpies around 90–100 J g⁻¹.^[13] Both amorphous metal oxide thin films and glassy materials show crystallization behavior that is purely driven by the reduction of the volume free energy in the transformation of amorphous to crystalline.^[13] A metal oxide thin film crystallizes directly within the solid structure when heated above its film deposition temperature similar to a glass thin film. These metal oxide thin films exhibit dense and amorphous microstructures directly after film deposition whereby they remain in a solid state for the full transition from the amorphous to the fully crystalline state. Consequently, heating rates greatly affect the degree of crystallinity of metal oxide thin films and predictions of microstructure evolution through temperature-time annealing are of major importance for their integration and operation as functional layers in microelectromechanical

[*] Dr. J. L. M. Rupp, B. Scherrer, N. Schäuble, Prof. L. J. Gauckler
Department of Materials
ETH Zurich
ETH Zurich Wolfgang-Pauli-Str.10 CH-8093 Zurich (Switzerland)
E-mail: jennifer.rupp@mat.ethz.ch

DOI: 10.1002/adfm.201000377

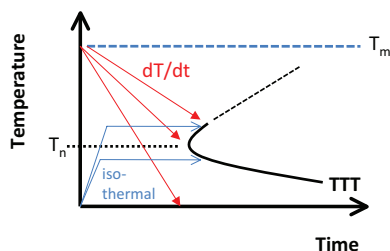


Figure 1. Classical TTT diagram for steel, alloys, or glass-based systems, such as metallic glasses or glass-ceramics. The TTT curve indicates in general phase transformations with respect to the cooling rate (dT/dt) of the material from the melt state, indicated by its melting temperature T_m . The minimal cooling rate for equal phase formation with respect to time–temperature is given by the nose temperature T_n . The latter variable is directly related to the melting temperature and, in accordance to Vogel-Fulcher, to the viscosity of the glass-based system.

systems (MEMS) devices, such as, inorganic sensors,^[17,18] micro-Solid Oxide Fuel Cells (micro-SOFCs),^[19–25] and oxygen pumps. For the latter applications, ceria-based films are currently being introduced as resistive sensing layers and ion-conducting low-temperature electrolyte materials.^[18,24–26] Therefore, TTT diagrams may be seen as a suitable approach for a better thermal engineering of metal oxide thin films in MEMS fabrication or during operation at elevated temperatures.

It has been shown that a large variety of processing possibilities exist to deposit solid, amorphous, metal oxide thin films such as precipitation-based film processing,^[27–29] for example, spray pyrolysis, sol-gel, or flame-spray processing, and vacuum-based techniques,^[27,30] for instance, pulsed laser deposition (PLD) or physical vapor deposition (PVD). All processing methods have in common that the amorphous thin films crystallize upon annealing at temperatures above the deposition temperature. Therefore, these films substantially differ from conventional powder processed-ceramics where crystallization is accomplished prior to densification during sintering of the material.

Crystallization kinetics of thin films are strongly dependent on the processing parameters and the chemistry of the materials. Two main classes of metal oxide film preparation technologies can be identified, namely, precipitation-based versus vacuum-processed thin films. Precipitation-based technologies rely on a wet-chemistry technique incorporating some of the solvent in the amorphous material, whereas vacuum-processed metal oxide thin films do not contain solvents but instead they retain oxygen vacancies after deposition. It has recently been reported that organic residuals affect the disorder state of amorphous precipitation-based films acting as space filler in the metal oxide network and affecting the crystallization history.^[31] In contrast to precipitation-based film techniques, vacuum processing always involves a slight reduction and non-stoichiometric change of the metal oxide thin film. The initial defect states (vacancy concentration and microstrain) within an amorphous metal oxide thin film can vary dramatically depending on the film processing technology and thus affect the crystallization kinetics. Moreover, the crystallization temperature range is related to the deposition temperature of the thin films.

In this paper, we focus on metal oxide thin films of the ceria system processed via a precipitation-based method of spray pyrolysis. Ceria-based ceramics exhibit a single cubic phase of the CaF_2 structure^[32] and no symmetry changes of the crystalline phase occur during crystallization. It is known that doping of the ceria lattice with trivalent cations results in solute drag impeding the grain growth. Doped ceria materials exhibit lower grain growth kinetics compared to pure ceria.^[14–16,33–36] However, the role of solute doping on the crystallization kinetics of simple metal oxide thin films, such as the ceria system, is still unclear. It is known for glass-ceramics, as well as metallic glasses, that doping can dramatically affect the ambient melt and glass-transition temperature and, consequently, the crystallization. Thus, it is reasonable to assume that the crystallization kinetics of a metal oxide such as ceria could be affected by doping as well.

Recently, primary crystallization kinetics of pure ceria thin films deposited in the amorphous state by spray pyrolysis has been reported.^[31] The Kissinger activation energy varied up to 10% between 90–100 J g^{-1} (for 3 $^\circ\text{C min}^{-1}$) and the effective crystallization activation energy ranged from 2.2–2.6 eV for undoped ceria depending on the initially used glycol in the film preparation.^[31,37–39] Fu and co-workers studied crystallization kinetics of pure and doped ceria gels and reported the impact of lanthanoid group elements Gd,^[40] La,^[41] and Y^[42] as dopants on the crystallization of 20 mol%-doped ceria powders during calcination. They found crystallization activation energies of 0.9 eV,^[40] 1.8 eV,^[41] and 2 eV,^[42] respectively. Summarizing these activation energies for ceria powders and its solutes one may conclude that the activation energy of these powders for crystallization is the lowest for gadolinia-doped materials. This represents the solute with the smallest lattice mismatch towards the ceria lattice and, thus, the best solubility in this lattice. These gels and calcined powders are indeed closest to the class of precipitation-based ceramic thin films, namely, to reported spray pyrolysis thin films^[31,43] fabricated by wet-chemistry processing at low temperatures over an alcohothermal, hydrothermal, or pyrolysis reaction.^[44–46]

This paper proposes primary TTT diagrams for the crystallization of metal oxide thin films using the example of ceria and its gadolinia solutes. The similarities and differences of these TTT diagrams with those for glass-based systems are discussed. For this, differential scanning calorimetry (DSC) experiments were performed on precipitation-based spray pyrolysis thin films of pure ceria and 20 mol% gadolinia doping to evaluate the impact of a strong solute doping on the crystallization of an originally amorphous metal oxide thin film. Finally, a schematic TTT diagram and model of the crystallization for metal oxide thin films with and without solutes are discussed.

2. Results and Discussion

2.1. Thin Film Microstructures, Crystallization, and Grain Growth

Scanning electron microscopy (SEM) images of the microstructure of the undoped and 20 mol% gadolinia-doped ceria spray pyrolysis thin films are shown in Figure 2. The thin films are shown after annealing at 1000 $^\circ\text{C}$ (ramping up to this

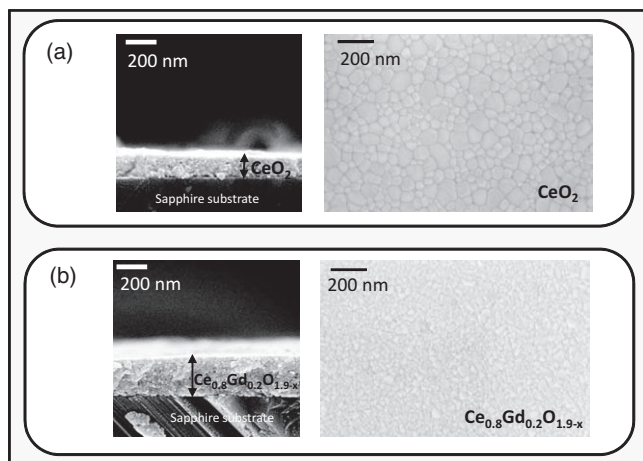


Figure 2. SEM cross sections and top-view images of spray-pyrolysis CeO_2 and $\text{Ce}_{0.8}\text{Gd}_{0.2}\text{O}_{1.9-x}$ thin films on sapphire substrates: a) CeO_{2-x} and b) $\text{Ce}_{0.8}\text{Gd}_{0.2}\text{O}_{1.9-x}$. The thin films are shown after annealing at 1000 °C for 0 h with $\pm 3 \text{ °C min}^{-1}$ heating and cooling rate.

temperature and immediately cooling down without holding at this temperature, 3 °C min^{-1} heating and cooling rate). The thin films are crack-free, and dense and are roughly 200–300 nm in film thickness. The undoped ceria thin films reveal larger average grain sizes around 140 nm, whereas a roughly 80 nm average grain size is seen for the doped thin films. Similar microstructures have been obtained before for ceria spray-pyrolysis thin films.^[35,36,47]

The crystallization kinetics of the originally amorphous as-deposited CeO_{2-x} and $\text{Ce}_{0.8}\text{Gd}_{0.2}\text{O}_{1.9-x}$ thin films were measured via DSC analysis and are displayed in **Figure 3**. This exothermic DSC heat release reflects the full transformation from amorphous to crystalline and is proportional to the crystallization enthalpy of the material.^[48] A single broad crystallization DSC peak starting at 400 °C was measured for ceria-based spray pyrolysis thin films independent of the gadolinia doping. The crystallization end temperature of the DSC exotherms was different for the undoped and gadolinia-doped thin films, namely, 950 and 1100 °C, respectively. Doping the thin film with 20 mol% gadolinia retards the overall crystallization and

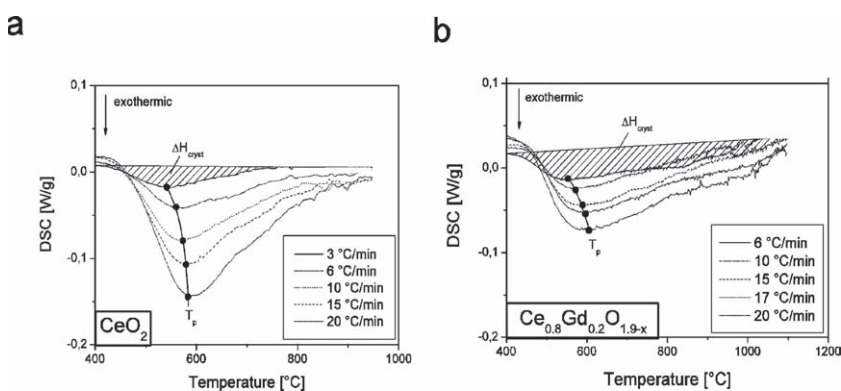


Figure 3. Non-isothermal crystallization monitored by the exothermic heat release in DSC experiments of CeO_2 and $\text{Ce}_{0.8}\text{Gd}_{0.2}\text{O}_{1.9-x}$ thin films produced by spray pyrolysis.

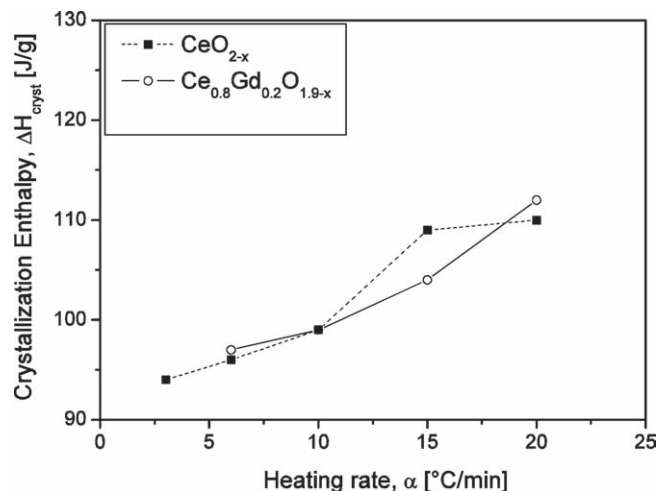


Figure 4. Crystallization enthalpy ΔH_{crist} for CeO_2 and $\text{Ce}_{0.8}\text{Gd}_{0.2}\text{O}_{1.9-x}$ thin films produced by spray pyrolysis.

shifts the crystallization end temperature at which full crystallinity is reached. The original amorphous state of the thin films directly after film deposition has been characterized before by Raman spectroscopy,^[31] X-ray diffraction (XRD),^[13,35] and transmission electron microscopy (TEM)^[13,49] analysis.

The crystallization enthalpy, ΔH_{crist} , and crystallization peak temperature, T_p , of both thin film materials for different heating rates are displayed in **Figure 4** and **5**, respectively. The crystallization enthalpies for the CeO_{2-x} and $\text{Ce}_{0.8}\text{Gd}_{0.2}\text{O}_{1.9-x}$ thin films are almost equal at 96 and 111 J g^{-1} for all different heating rates of 3 to 20 °C min^{-1} , as shown in Figure 4. The crystallization peak temperature increases from around 542 to 590 °C at equal heating rates, as shown in Figure 5. It is interesting to see that the crystallization enthalpy and peak temperature are almost equal for CeO_{2-x} and $\text{Ce}_{0.8}\text{Gd}_{0.2}\text{O}_{1.9-x}$ thin films for similar heating rates, even though a largely increased crystallization temperature regime (+150 °C) is found for the doped thin films.

Effective activation energies of crystallization were evaluated using the Kissinger equation^[50] and the results are presented in

Figure 6 for CeO_{2-x} and $\text{Ce}_{0.8}\text{Gd}_{0.2}\text{O}_{1.9-x}$. The activation energies of crystallization of CeO_{2-x} and $\text{Ce}_{0.8}\text{Gd}_{0.2}\text{O}_{1.9-x}$ were 2.2 and 1.6 eV, respectively. The crystallization activation energy of the undoped ceria thin film agrees with findings on previously studied ceria spray-pyrolysis thin films that reported 2.2 and 2.6 eV values depending on the organic compound used in the film preparation.^[31] Fu and co-workers reported an activation energy of 0.9 eV for calcined $\text{Ce}_{0.8}\text{Gd}_{0.2}\text{O}_{1.9-x}$ powders.^[40] Comparing their findings with crystallization activation energies determined via the Kissinger equation on yttria-stabilized zirconia powders of 0.6–1.3 eV and 2.4–3.5 eV for 3 and 8 mol% doping, respectively, shows that their reported activation energies are in a comparable range.

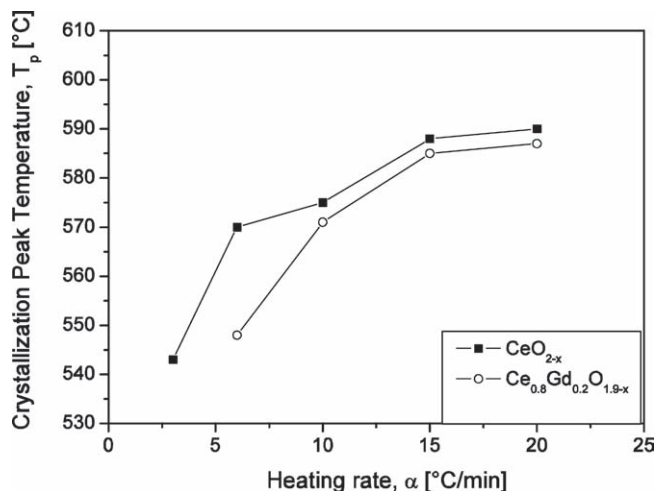


Figure 5. Crystallization peak temperature T_p for CeO_2 and $\text{Ce}_{0.8}\text{Gd}_{0.2}\text{O}_{1.9-x}$ thin films produced by spray pyrolysis.

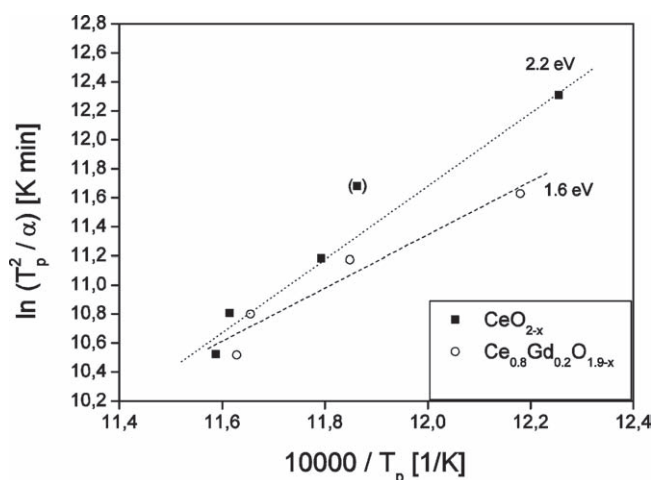


Figure 6. Kissinger plot of CeO_2 and $\text{Ce}_{0.8}\text{Gd}_{0.2}\text{O}_{1.9-x}$ thin films produced by spray pyrolysis. The crystallization peak temperature is denoted as T_p and the heating rate as α .

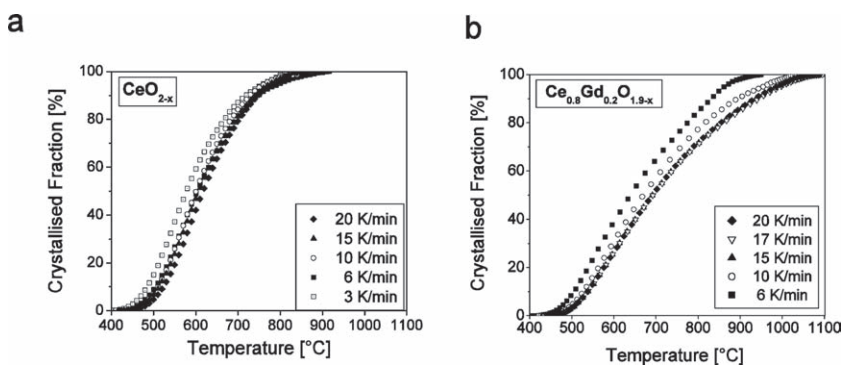


Figure 7. Non-isothermal crystallized fraction of CeO_2 and $\text{Ce}_{0.8}\text{Gd}_{0.2}\text{O}_{1.9-x}$ thin films produced by spray pyrolysis.

In **Figure 7** the crystallized fractions of material, evaluated from the integral fractions of the exothermic signals of the DSC experiments from **Figure 3**, are plotted against the annealing temperature. The sigmoidal shaped curves in **Figure 7a & b** correspond to those obtained for classical glass-ceramic transitions that are normally evaluated using the Johnson-Mehl-Avrami model.^[51,52] An almost linear correlation between the volume fraction that is crystallized and the annealing temperature is valid for the main part of the crystallization process. The two nonlinear parts reflect the nucleation process at low temperatures and the end of the crystallization process.^[53] The nucleation process occurs within a very short temperature interval between 400 to 530 °C, independent of doping.

It is found that the impact of the solute on the crystallization depends strongly on the temperature range with respect to the crystallization peak temperature T_p (**Figure 5**), namely: i) for $T < T_p$, $\text{Ce}_{0.8}\text{Gd}_{0.2}\text{O}_{1.9-x}$ and the undoped films show almost identical crystallization rates of 0.049 and 0.050 crystallized fraction per hour, as shown in **Figure 7**. In this initial stage the first crystals grow within the amorphous film and no impact of the solute is measured. ii) At temperatures around the crystallization peak temperature $T = T_p$ both thin films show a similar volume fraction of around 20% that is crystallized at $T_p = 540\text{--}590$ °C, for heating rates of 3–20 °C min^{-1} . iii) At temperatures higher than the peak temperatures of crystallization, $T > T_p$, the pure CeO_{2-x} shows a 0.42 crystallized fraction per hour, which is a much higher crystallization rate than that of $\text{Ce}_{0.8}\text{Gd}_{0.2}\text{O}_{1.9-x}$ with a rate of 0.27 crystallized fraction per hour. The 36% reduced crystallization rate of the doped film reveals the influence of solute drag on crystallization of the dopant gadolinium. A closer comparison of the two materials at 700 °C, the data in **Figure 7**, shows exemplary that 83% and 55% crystallized volume fractions were measured for the CeO_{2-x} and $\text{Ce}_{0.8}\text{Gd}_{0.2}\text{O}_{1.9-x}$ thin films, respectively.

In **Table 1**, the crystallization peak temperature, the crystallized volume fractions, and the average grain sizes are presented for CeO_{2-x} and $\text{Ce}_{0.8}\text{Gd}_{0.2}\text{O}_{1.9-x}$ thin films for non-isothermal crystallization at a heating rate of 6 °C min^{-1} . The table reveals for $T < T_p$ that the crystallized volume fraction and the actual average grain size of the thin films are almost equal for both materials. However, for $T > T_p$, the crystallized volume fraction and the actual grain size are both strongly reduced by the solute. The undoped ceria reveals larger grain sizes and especially increased volume fractions that are crystallized at the same temperature as compared to the 20 mol% doped films.

The LSW theory^[54,55] on Ostwald ripening describes the growth of particles in a dilute dispersion as a two-step crystallization and growth process.^[56] In a first step, a crystallization stage, particle growth proceeds through Ostwald ripening controlled by the interface reactions between a single particle and the surrounding media. At this stage the growth is driven by the average concentration of the solute in the surrounding area of the particle. In a second step, a growth

Table 1. Non-isothermal grain growth and crystallization of CeO₂ and Ce_{0.8}Gd_{0.2}O_{1.9-x} thin films produced by spray pyrolysis with respect to temperature for 6 °C min⁻¹ heating. The crystallization peak temperature, T_p is also included.

Temperature [°C]	CeO ₂		Ce _{0.8} Gd _{0.2} O _{1.9-x}	
	Crystallinity [%]	Average grain size [nm]	Crystallinity [%]	Average grain size [nm]
20	8	7	4	8
400	9	7	4	8
500	12	16		
600	22	45	10	39
700	65	88	13	55
Crystallization peak temperature, T_p		569		550

stage, neighboring particles touch each other and start to form grain boundaries. Grain growth in this stage is purely grain-curvature dominated and is no longer controlled by mass transport from the surrounding matrix. A similar model can be applied to the crystallization and growth of grains in the present metal oxide thin films: in the first crystallization stage the grains are dispersed and isolated in the amorphous matrix and the crystallization and grain growth is purely driven by the balance between the volume free energy because of crystallization and the increase in interfacial energy at the crystalline/amorphous phase boundary. In this early stage the crystallization rate is low and the cerium as well as gadolinium dopant atoms are consumed from the amorphous phase for crystal formation. The crystallization rate is purely determined by the interfacial reaction rate of the atoms in the amorphous matrix and the crystallites' surfaces. Once the crystallization peak temperature is reached at T_p a volume fraction of about 0.2 is crystallized and the grains start to percolate and cluster. Then, grain coarsening occurs by consuming amorphous matrix atoms, which is accompanied by moving grain boundaries among the grains. In this stage grain growth occurs at the expense of the accrue of other grains and the grain growth kinetics becomes dependent on solute drag. This is also reflected in the reduced crystallization rate.

2.2. TTT-Diagrams

TTT-diagrams are presented for amorphous thin films in **Figure 8**. Indicated in the plot are the amorphous range and the iso-crystalline lines representing equal degrees of fractions of crystallized material for constant conversion rates.

The specific characteristic temperatures are those of the thin-film deposition temperature (T_d) and the crystallization peak temperature (T_p). The original single data points were taken from both previous reports and our own study using non-isothermal and isothermal DSC crystallization experiments, XRD data, and TEM analysis of CeO_{2-x}^[13,31,36] and 20 mol% gadolinia-doped ceria thin films^[35,49] and the data and their origin are summarized in **Table 2**.

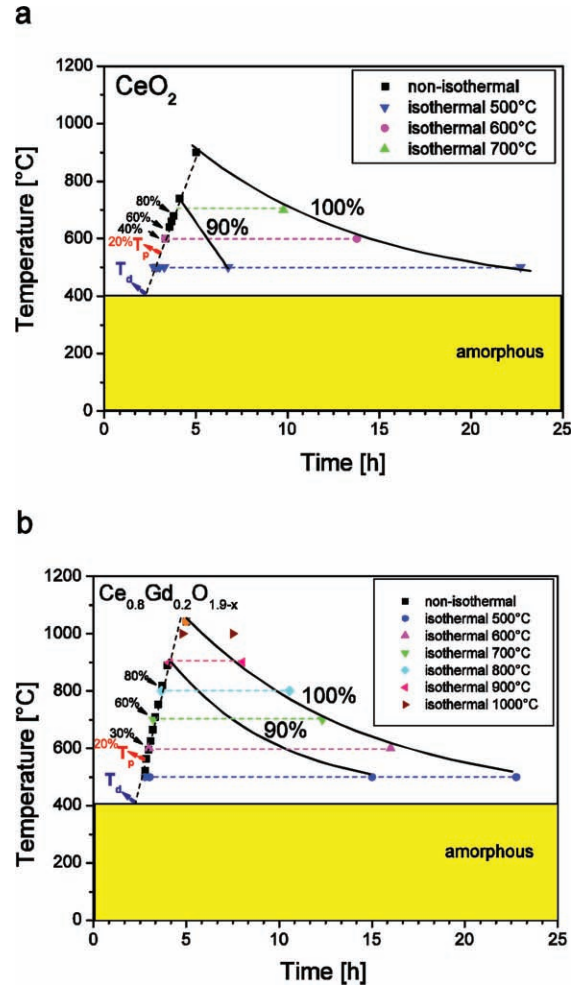


Figure 8. TTT diagrams for the originally amorphous, undoped ceria metal oxide thin films and the 20 mol% gadolinia doped-solute solution. The plots display the thermokinetics of crystallization of the original amorphous thin films indicated by the degree of crystallinity in percentage. The important key temperatures for their crystallization are the deposition temperature (T_d), crystallization peak temperature (T_p) (determined by DSC from the exothermic heat loss^[13]) and the crystallization end temperature (T_e). For $T < T_p$ mostly nucleation is ongoing and the crystallization rates are similar for both the undoped and doped thin films. However, for $T > T_p$ the crystallization rate of the doped thin film is strongly suppressed and T_e is shifted to higher temperatures (by roughly 200 °C). These TTT diagrams can now be used to predict the crystallization degree of a thin film for pure isothermal or non-isothermal annealing, as well as their combination, and may give suitable guidance for the introduction of these thin films in MEMS, where isothermal heating steps are needed to restrict the overall process temperature below that where substrate damage occurs (e.g., oxidation of silicon around 800 °C). Original data points are listed in Table 1.

The thin films nucleate readily at 410 °C, which is slightly above the thin-film deposition temperature $T_d = 390$ °C, **Figure 8**. In contrast to classical glass-ceramic or metallic-glass TTT diagrams, where the cooling curves are registered for transformation from the undercooled liquid to the crystalline state, the thin films crystallize upon heating to temperatures higher than their thin-film deposition

Table 2. Data origin for determining the degree of crystallinity for the TTT diagrams of CeO_{2-x} and $\text{Ce}_{0.8}\text{Gd}_{0.2}\text{O}_{1.9-x}$ thin films made by the precipitation-based method of spray pyrolysis (Figure 8).

CeO_{2-x}			$\text{Ce}_{0.8}\text{Gd}_{0.2}\text{O}_{1.9-x}$		
Crystallization experiment			Crystallization experiment		
non-isothermal	isothermal	Ref.	non-isothermal	isothermal	Ref.
3–20 °C/min, DSC study	–	this study	3–20 °C/min, DSC and TEM study	–	this study, [50]
–	500–900 °C DSC, Raman, XRD and TEM studies	[13, 29]	–	500–1100 °C DSC, XRD and TEM studies	this study, [36]

temperature ($T > T_d$). In the present TTT diagrams the impact of the solute is clearly visible for temperatures higher than the crystallization peak temperature, $T > T_p$. Below T_p crystallization proceeds mostly at a similar rate for both thin films with respect to non-isothermal, as well as isothermal annealing. However, the choice of heating rate for $T > T_p$ greatly affects the degree of crystallinity for the doped material. The $\text{Ce}_{0.8}\text{Gd}_{0.2}\text{O}_{1.9-x}$ thin films need a much longer time under isothermal heating to reach the same fraction of crystallization as compared to pure CeO_{2-x} , or higher temperatures for non-isothermal heating. This is similar to a glass-based system, where the introduction of solutes shifts the nose of the “C-type” TTT curve to higher temperatures, thus providing more time to undergo phase transition. This reveals that much lower heating rates are required to crystallize the pure ceria compared to the Gd-containing CeO_2 solid solution. TTT

diagrams clearly reveal the temperature-time regions in which the solute influences the crystallization rate. Therefore, these TTT diagrams are a useful guide for the evaluation of solute-drag effects on the grain-growth kinetics of thin films, similar to the standard TTT diagrams already existing for glass-based systems.

On the basis of the current TTT diagrams for ceria-based thin films one can, for example, determine that a low heating rate (e.g., $<1 \text{ °C min}^{-1}$) or an isothermal dwell procedure (e.g., isothermal hold for 15 h at 700 °C) is required to obtain fully crystalline $\text{Ce}_{0.8}\text{Gd}_{0.2}\text{O}_{1.9-x}$ thin films. In the present example conventional heating rates $>6 \text{ °C min}^{-1}$ only produce fully crystalline films at temperatures of 1000 °C or above. A schematic concept of the present results from the TTT diagrams for crystallization of metal oxide thin films is shown in Figure 9.

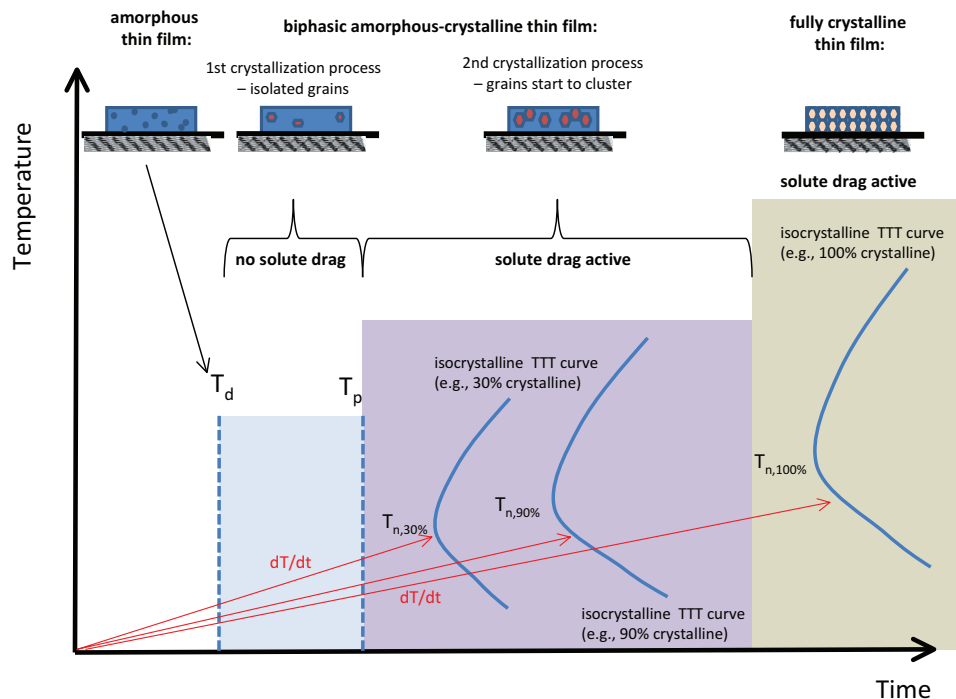


Figure 9. TTT diagram for metal oxide thin film. The TTT curves indicate phase transformations with respect to the heating rate of the thin film. The minimal heating rate for equal phase formation with respect to time–temperature is given by the nose temperature T_n of an isocrystalline “C-type” TTT curve. The thin-film deposition temperature, T_d , and the DSC crystallization peak temperature, T_p , are indicated.

3. Conclusions

The importance of primary TTT diagrams for the crystallization of amorphous metal oxide thin films, for CeO_{2-x} and its gadolinia solute solutions is proven to give suitable thermokinetic guidance for usage of functional thin films in microelectromechanical systems (MEMS). These metal oxide thin films deposited by spray pyrolysis exhibit dense and amorphous microstructures directly above the film deposition and they remain in the solid state for the full transition from amorphous to fully crystalline. In the first crystallization stage single crystals form in the amorphous thin-film matrix, and crystallization, as well as grain growth proceed in a solute-independent way. Once the crystallization peak temperature, T_p , is reached the solute slows down the grain growth, as well as the crystallization of the thin film. For $T > T_p$, dopant-dependent crystallization rates of 0.42 and 0.27 crystallized fraction per hour were determined for CeO_{2-x} and $\text{Ce}_{0.8}\text{Gd}_{0.2}\text{O}_{1.9-x}$ thin films under non-isothermal heating at $6\text{ }^\circ\text{C min}^{-1}$. The exemplary TTT diagrams of the two thin film materials show isocrystalline lines (a constant degree of crystallinity with respect to heating), as well as the important thin-film characteristics, such as the crystallization peak temperature, T_p , thin-film deposition temperature, T_d , and the presence of the fully amorphous and crystalline phases. Comparison of the TTT diagrams for the undoped and doped thin films reveals that only for $T > T_p$ the TTT curves of the doped film shift to longer times and higher temperatures once crystallizing grains start to cluster.

The TTT diagrams for these metal oxide thin films differ from those of metals or glass-based systems as the crystallization history is heating (and not cooling)-rate dependent. This difference can be attributed to the film characteristics, such as the initial deposition temperature and the crystallization peak temperature, which are given by the choice of film processing, and the fact that the whole crystallization process occurs in the solid state.

For the field of MEMS engineering TTT diagrams of metal oxide thin films are of high relevance for thermal processing of the devices. We have successfully demonstrated the usage and importance of TTT diagrams such as the one for the $\text{Ce}_{0.8}\text{Gd}_{0.2}\text{O}_{1.9-x}$ spray-pyrolysis thin films for thermal engineering of these thin films in micro-SOFCs. The TTT diagrams illustrate that extremely low heating rates, for instance, $1\text{ }^\circ\text{C min}^{-1}$ or lower, or multi-step annealing with isothermal holds at temperatures below $800\text{ }^\circ\text{C}$ are required for the realization of purely crystalline $\text{Ce}_{0.8}\text{Gd}_{0.2}\text{O}_{1.9-x}$ electrolyte thin films in order to avoid damaging of the wafer substrate of the fuel cell. Conventional heating at higher heating rates, for example at $3\text{--}6\text{ }^\circ\text{C min}^{-1}$, usually used in the fabrication of micro-SOFCs, would have to be carried out at $1100\text{ }^\circ\text{C}$ to assure the full crystallinity of the electrolyte film. It is clear that such high temperatures would severely damage the wafer substrate and, therefore, better thermal engineering on the basis of these TTT diagrams should be carried out. It is therefore recommended to encourage the establishment and use of TTT diagrams for metal oxide thin films to allow for better MEMS engineering in the future.

4. Experimental Section

Thin Film Preparation: Ceria spray-pyrolysis precursor solutions were made of 0.1 M cerium nitrate (Alfa Aesar, 99% purity) dissolved in

$10:90\text{ (v/v)}$ water/tetraethylene glycol (Aldrich, > 99% purity). For the gadolinia-doped thin films the same solvents were used and 0.02 M gadolinium chloride (Alfa Aesar, 99% purity) was dissolved with 0.08 M of the cerium nitrate salt. These precursor solutions were fed to a spray gun (Compact 2000 KM, Böllhoff Verfahrenstechnik, Germany) with a liquid flow rate of 5 mL h^{-1} and atomized at 1 bar standard atmospheric pressure. The droplets produced in this manner were sprayed on a heated sapphire single-crystal substrate (Stettler, Switzerland) at $390 \pm 5\text{ }^\circ\text{C}$ for 1.45 h . The working distance between the spray nozzle and the hot plate was kept at 39 cm during the whole experiment. The spray-pyrolysis process is described in further detail elsewhere.^[7–9] After spray pyrolysis the thin films were amorphous and could be converted to biphasic amorphous-nanocrystalline or totally nanocrystalline films by annealing at temperatures higher than the deposition temperature.^[10,11]

Crystallization: Crystallization of the amorphous thin films during annealing was measured using calibrated differential scanning calorimetry (DSC/TG, Netzsch STA 449C) experiments. In these measurements the degree of crystallinity was determined from the exothermic heat loss results.^[57] In order to quantify the DSC results, the instrument was calibrated with calibration standards (Netzsch 6.223.5–91.2) of known heat absorption for melting points or phase changes. The as-deposited amorphous CeO_2 thin films were scratched off from the sapphire substrate and the obtained powder was analyzed by DSC. The powder was always enclosed in a Pt pan with a lid and measured against an empty Pt pan with a lid as a reference under static air atmosphere.

In the case of continuous heating, $50 \pm 1\text{ mg}$ of amorphous CeO_2 powder was measured at different heating rates ranging from $3\text{--}20\text{ }^\circ\text{C min}^{-1}$. A subsequent correction measurement for quantitative DSC analysis using a totally crystallized, spray-pyrolysis CeO_{2-x} powder of the same mass under equivalent experimental conditions was performed. The result of this experiment was recorded and subtracted from the measurement of the originally amorphous powder.

Grain Growth: The average grain size was determined by X-ray diffraction (XRD, Bruker AXS D8 Advance). The development of line widths of the Bragg peaks during in-situ annealing in a furnace (Anton Paar HTK 1200) provided information on the average grain size development. Diffracted X-rays from the sample were detected by a position-sensitive detector (Braun PSD ASA-S). The XRD setup was equipped with a Cu radiation source ($\lambda = 0.15404\text{ nm}$) operated at 40 kV and 40 mA followed by a $\text{K}\alpha_1\text{-Ge}$ monochromator (Bruker AXS). The average grain size was determined from the full width at half maximum (FWHM), by using Fourier analysis of the XRD peaks, refined by a split Pearson 7 function (Software EVA 6.0). The FWHM resulted from instrumental broadening and from the microstructure of the film. The instrumental peak broadening of the diffractometer was determined by measuring a commercially available microcrystalline and stress-free CeO_2 powder of large particles (Alfa Aesar, purity 99.99%). The instrumental broadening could then be eliminated from the FWHM using the Warren and Bischoff equation.^[58] The average grain size was then calculated according to the Scherrer equation.^[59,60]

Acknowledgements

Financial support from the Competence Centre for Materials Science and Technology (CCMX) for funding the NANCER consortium over the last three years is gratefully acknowledged.

Received: February 26, 2010
Published online: July 26, 2010

- [1] D. R. Uhlmann, *J. Non-Cryst. Solids* **1972**, *22*, 367.
- [2] G. F. Van Der Voort, *Atlas of Time-Temperature Diagrams for Nonferrous Alloys*, ASM International **1991**.
- [3] J. F. Löffler, *Bulk Metallic Glasses: Intermetallics* **2003**, *11*, 529.
- [4] W. L. Johnson, *Curr. Opin. Solid State Mater. Sci.* **1996**, *1*, 383.

- [5] Z. Strnad, *Glass Science and Technology* 8, Elsevier, The Netherlands **1986**, Ch. 1.
- [6] I. Gutzow, D. Kashchiev, I. Avramov, *J. Non-Cryst. Solids* **1985**, 73, 477.
- [7] I. Gutzow, I. Avramov, K. Kästner, *J. Non-Cryst. Solids* **1990**, 123, 97.
- [8] M. C. Weinberg, *Thermochim. Acta* **1996**, 280–281, 63.
- [9] P. H. Gaskell, *J. Non-Cryst. Solids* **1997**, 222, 1–12.
- [10] F. C. Campbell, in *Manufacturing Technology for Aerospace Structural Materials*, Elsevier Science, Oxford, UK **2006**, p. 541.
- [11] H. Vogel, *Phys. Z.* **1921**, 22.
- [12] G. S. Fulcher, *J. Am. Ceram. Soc.* **1925**, 8, 339.
- [13] J. L. M. Rupp, B. Scherrer, A. Harvey, L. J. Gauckler, *Adv. Funct. Mater.* **2009**, 19, 2790.
- [14] E. Jud, C. B. Huwiler, L. J. Gauckler, *J. Ceram. Soc. Jpn.* **2006**, 114, 963.
- [15] E. Jud, L. J. Gauckler, *J. Electroceram.* **2005**, 14, 247.
- [16] T. S. Zhang, J. Ma, Y. J. Leng, S. H. Chan, P. Hing, J. A. Kilner, *Solid State Ionics* **2004**, 168, 187.
- [17] H. L. Tuller, *Electrochim. Acta* **2003**, 48, 2879.
- [18] H. L. Tuller, R. Mlac, *Curr. Opin. Solid State Mater. Sci.* **1998**, 3, 501.
- [19] H. Huang, M. Nakamura, P. C. Su, R. Fasching, Y. Saito, F. B. Prinz, *J. Electrochem. Soc.* **2007**, 154, B20.
- [20] J. H. Shim, C.-C. Chao, H. Huang, F. B. Prinz, *Chem. Mater.* **2007**, 19, 3850.
- [21] J. L. M. Rupp, U. P. Muecke, P. C. Nalam, L. J. Gauckler, *J. Power Sources* **2010**, 195, 2669.
- [22] A. Bieberle-Hütter, A. Infortuna, U. P. Muecke, J. L. M. Rupp, L. J. Gauckler, S. Rey-Mermet, P. Mural, N. R. Bieri, N. Hotz, M. J. Stutz, D. Poulikakos, P. Heeb, P. Müller, A. Bernard, R. Gmür, T. Hocker, *J. Power Sources* **2008**, 177, 123.
- [23] U. P. Muecke, D. Beckel, A. Bernard, A. Bieberle-Hütter, S. Graf, A. Infortuna, J. L. M. Rupp, J. Schneider, P. Müller, J. Gauckler, *Adv. Funct. Mater.* **2008**, 18, 3158.
- [24] A. Evans, A. Bieberle-Hütter, H. Galinski, J. L. M. Rupp, T. Ryll, S. Barbara, R. Tölke, L. J. Gauckler, *Chem. Monthly* **2009**, 140, 975.
- [25] A. Evans, A. Bieberle-Hütter, J. L. M. Rupp, L. J. Gauckler, *J. Power Sources* **2009**, 194, 119.
- [26] H. L. Tuller, *Solid State Ionics* **2000**, 131, 143.
- [27] D. Beckel, A. Bieberle-Hütter, A. Harvey, A. Infortuna, U. P. Muecke, M. Prestat, J. L. M. Rupp, L. J. Gauckler, *J. Power Sources* **2007**, 173, 325.
- [28] N. I. Karageorgakis, A. Heel, J. L. M. Rupp, M. Aguirre, T. Graule, L. J. Gauckler, *Adv. Funct. Mater.*, in press.
- [29] A. O. Stoermer, J. L. M. Rupp, L. J. Gauckler, *Solid State Ionics* **2006**, 177, 2075.
- [30] S. Heiroth, T. Lippert, A. Wokaun, M. Döbeli, J. L. M. Rupp, B. Scherrer, L. J. Gauckler, *J. Eur. Ceram. Soc.* **2010**, 30, 489.
- [31] J. L. M. Rupp, B. Scherrer, L. J. Gauckler, *Phys. Chem. Chem. Phys.*, in press, DOI: 10.1039/b920971a.
- [32] M. Mogensen, N. M. Sammes, G. A. Tompsett, *Solid State Ionics* **2000**, 129, 63.
- [33] H. Inaba, T. Nakajima, H. Tagawa, *Solid State Ionics* **1998**, 106, 263.
- [34] D. D. Upadhyaya, R. Bhat, S. Ramanathan, S. K. Roy, H. Schubert, G. Petzow, *J. Eur. Ceram. Soc.* **1994**, 14, 337.
- [35] J. L. M. Rupp, A. Infortuna, L. J. Gauckler, *Acta Mater.* **2006**, 54, 1721.
- [36] J. L. M. Rupp, L. J. Gauckler, *Solid State Ionics* **2006**, 177, 2513.
- [37] J. Chandradass, B. Nam, K. H. Kim, *Colloids Surf. A: Physicochem. Eng. Aspects* **2009**, 348, 130.
- [38] B. Ksapabutr, E. Gulari, S. Wongkasemjit, *Mater. Chem. Phys.* **2006**, 99, 318.
- [39] M. Kamruddin, P. K. Ajikumar, R. Nithya, G. Mangamma, A. K. Tyagi, B. Raj, *Powder Technol.* **2006**, 161, 145.
- [40] Y. P. Fu, Y. C. Liu, S. H. Hu, *Ceram. Int.* **2009**, 35, 3153.
- [41] Y. P. Fu, S. H. Chen, F. Y. Tsai, S. H. Hu, *Ceram. Int.* **2009**, 35, 609.
- [42] Y. P. Fu, S. B. Wen, C. W. Tseng, F. Y. Tsai, C. S. Hsu, B. L. Liu, *Jpn. J. Appl. Phys.* **2008**, 47, 5567.
- [43] J. L. M. Rupp, T. Drobek, A. Rossi, L. J. Gauckler, *Chem. Mater.* **2007**, 19, 1134.
- [44] Q. Yuan, H.-H. Duan, L.-L. Li, L.-D. Sun, Y.-W. Zhang, C.-H. Yan, *J. Colloid Interface Sci.* **2009**, 335, 151.
- [45] P. Bowen, C. Carry, *Powder Technol.* **2002**, 128, 248.
- [46] K. Kendall, *Powder Technol.* **1989**, 58, 151.
- [47] J. L. M. Rupp, A. Infortuna, L. J. Gauckler, *J. Am. Ceram. Soc.* **2007**, 90, 1792.
- [48] M. M. R. Boutz, A. J. A. Winnubst, A. J. Burggraaf, *J. Eur. Ceram. Soc.* **1994**, 13, 89.
- [49] J. L. M. Rupp, C. Solenthaler, P. Gasser, U. P. Muecke, L. J. Gauckler, *Acta Mater.* **2007**, 55, 3505.
- [50] H. E. Kissinger, *J. Res. Natl. Bur. Stand.* **1956**, 157.
- [51] M. Avrami, *J. Chem. Phys.* **1939**, 7, 1103.
- [52] M. Avrami, *J. Chem. Phys.* **1941**, 9, 177.
- [53] K. A. Jackson, *Kinetic Processes*, Wiley-VCH, Weinheim, Germany **2004**, Ch. 15.3, p. 199.
- [54] C. Wagner, *Z. Electrochem.* **1961**, 65, 581.
- [55] I. M. Lifshitz, *Phys. Chem. Solids* **1961**, 19, 35.
- [56] M. N. Rahaman, in *Ceramic Processing and Sintering*, Marcel Dekker, Dordrecht, The Netherlands **1995**, Ch. 9, pp. 642–644.
- [57] C. Michaelson, M. Dahms, *Thermochim. Acta* **1996**, 288, 9.
- [58] C. N. J. Wagner, E. N. Aqua, *J. Less Common Metals* **1965**, 8, 51.
- [59] P. Scherrer, *Nachr. Ges. Wiss. Göttingen, Math.-Phys. Kl.* **1918**, 1, 98.
- [60] A. J. C. Wilson, *Acta Crystallogr.* **1949**, 2, 318.